

## Unveiling the Chemical and Morphological Features of Sb–SnO<sub>2</sub> Nanocrystals by the Combined Use of High-Resolution Transmission Electron Microscopy and ab Initio Surface Energy Calculations

Daniel G. Stroppa,<sup>†</sup> Luciano A. Montoro,<sup>†</sup> Armando Beltrán,<sup>‡</sup> Tiago G. Conti,<sup>§</sup>  
Rafael O. da Silva,<sup>§</sup> Juan Andrés,<sup>‡</sup> Elson Longo,<sup>§</sup> Edson R. Leite,<sup>§</sup> and  
Antonio J. Ramirez<sup>\*†</sup>

Brazilian Synchrotron Light Laboratory, 13083-970 Campinas, SP, Brazil, Departament de Química Física i Analítica, Universitat Jaume I, 12071 Castellón de la Plana, Spain, and Department of Chemistry, Federal University of São Carlos, 13565-905 São Carlos, SP, Brazil

Received July 22, 2009; E-mail: ramirez@Inls.br

**Abstract:** Modeling of nanocrystals supported by advanced morphological and chemical characterization is a unique tool for the development of reliable nanostructured devices, which depends on the ability to synthesize and characterize materials on the atomic scale. Among the most significant challenges in nanostructural characterization is the evaluation of crystal growth mechanisms and their dependence on the shape of nanoparticles and the distribution of doping elements. This paper presents a new strategy to characterize nanocrystals, applied here to antimony-doped tin oxide (Sb–SnO<sub>2</sub>) (ATO) by the combined use of experimental and simulated high-resolution transmission electron microscopy (HRTEM) images and surface energy ab initio calculations. The results show that the Wulff construction can not only describe the shape of nanocrystals as a function of surface energy distribution but also retrieve quantitative information on dopant distribution by the dimensional analysis of nanoparticle shapes. In addition, a novel three-dimensional evaluation of an oriented attachment growth mechanism is provided in the proposed methodology. This procedure is a useful approach for faceted nanocrystal shape modeling and indirect quantitative evaluation of dopant spatial distribution, which are difficult to evaluate by other techniques.

### Introduction

The development and implementation of new applications for nanostructured materials is, in many cases, closely linked to the ability to describe, model, and control nanocrystal morphology during the synthesis process, especially by the bottom-up approach.<sup>1</sup> Hence, the successful application of nanocrystals as building blocks for the development of novel materials requires control over the shape and the assembly of those nanocrystals. Crystal modeling<sup>2–4</sup> is therefore a unique tool due to its wide application in the prediction of crystal shapes, growth process, and the resulting properties of an unlimited number of systems.

A key subject in materials chemistry and a major issue in crystal modeling, particularly for nanocrystals synthesis, is the strong influence of the chemical environment and synthesis parameters that determine the surface chemistry and crystal

morphology. Several cases reported in the literature show that organic and/or inorganic additives<sup>5–7</sup> and solvents<sup>8</sup> can determine crystal growth and final morphology. Those studies indicate that additives act as selective poisoning agents, shifting the configuration of the nanocrystal surface energy, defining crystal habit and preferential growth directions. However, the role of synthesis parameters on the resulting nanocrystal features is complex and still not fully understood.

In recent years, advanced tools<sup>9–13</sup> have been developed for nanocrystal characterization in order to obtain accurate chemical, structural, and morphological information, such as crystal-

<sup>†</sup> Brazilian Synchrotron Light Laboratory.

<sup>‡</sup> Universitat Jaume I.

<sup>§</sup> Federal University of São Carlos.

- (1) Leite, E. R. In *Encyclopedia of Nanoscience and Nanotechnology*; Nalwa, H. S., Ed.; American Scientific Publishers: Los Angeles, CA, 2004; Vol. 6.
- (2) Barnard, A. S.; Kirkland, A. I. *Chem. Mater.* **2008**, *20* (17), 5460–5463.
- (3) Barnard, A. S.; Yeredla, R. R.; Xu, H. F. *Nanotechnology* **2006**, *17* (12), 3039–3047.
- (4) Wang, Z.L.; Feng, X. J. *Phys. Chem. B* **2003**, *107*, 13563–13566.

- (5) Puentes, V. F.; Krishnan, K. M.; Alivisatos, A. P. *Science* **2001**, *291* (5511), 2115–2117.
- (6) Polleux, J.; Pinna, N.; Antonietti, M.; Hess, C.; Wild, U.; Schlogl, R.; Niederberger, M. *Chem.—Eur. J.* **2005**, *11*, 3541–3551.
- (7) Yang, H. G.; Sun, C. H.; Qiao, S. Z.; Zou, J.; Liu, G.; Smith, S. C.; Cheng, H. M.; Lu, G. Q. *Nature* **2008**, *453* (7195), 638–641.
- (8) Grubbs, R. B. *Nat. Mater.* **2007**, *6* (8), 553–555.
- (9) Huang, W. J.; Zuo, J. M.; Jiang, B.; Kwon, K. W.; Shim, M. *Nat. Phys.* **2009**, *5* (2), 129–133.
- (10) Jinschek, J. R.; Batenburg, K. J.; Calderon, H. A.; Kilaas, R.; Radmilovic, V.; Kisielowski, C. *Ultramicroscopy* **2008**, *108*, 589–604.
- (11) Arslan, I.; Yates, T. V. J. *Science* **2005**, *309*, 2195–2198.
- (12) Schamm, S.; Bonafos, C.; Coffin, H.; Cherkashin, N.; Carrada, M.; Ben Assayag, G.; Claverie, A.; Tence, M.; Colliex, C. *Ultramicroscopy* **2008**, *108*, 346–357.
- (13) Hansen, P. L.; Wagner, J. B.; Helveg, S.; Rostrup-Nielsen, J. R.; Clausen, B. S.; Topsøe, H. *Science* **2002**, *295* (5562), 2053–2055.

lographic habit, surface chemistry, and growth mechanisms from self-assembled arrangements. Although a number of techniques based on X-ray,<sup>9,14</sup> scanning probe microscopy,<sup>15</sup> and transmission electron microscopy (TEM)<sup>16–18</sup> have been successfully applied to retrieve compositional and morphological information about nanostructures, several challenges still remain, especially with regard to three-dimensional reconstruction and chemical mapping.

In this work we present a novel approach based on high-resolution transmission electron microscopy (HRTEM) characterization and surface energy ab initio calculation<sup>19</sup> (atomistic simulation). By combining information from HRTEM images of faceted nanocrystals, Wulff construction,<sup>20,21</sup> and surface energies obtained by atomistic simulation for selected facets, the 3D morphological and compositional features of ATO nanocrystals and their growth mechanisms were elucidated.

Among the transparent conductive oxides (TCO),<sup>22</sup> SnO<sub>2</sub> and its doped forms, such as FTO<sup>23</sup> (fluorine-doped tin oxide), ITO<sup>24</sup> (indium-doped tin oxide), and ATO<sup>25</sup> (antimony-doped tin oxide), have received special attention due to their unique electro-optical properties with applications in catalysis,<sup>26,27</sup> electronics,<sup>28</sup> optics,<sup>29</sup> and as gas sensors.<sup>30</sup> The antimony-doped tin oxide (Sb–SnO<sub>2</sub>) (ATO) nanocrystalline system<sup>31</sup> was chosen for this work because of the limitations for its comprehensive characterization by conventional and advanced techniques. These limitations are due to the reduced dimensions, small difference between the atomic weight of Sn and Sb, and the structural and chemical instability of these nanoparticles, which preclude long-duration TEM and/or scanning transmission electron microscopy (STEM) analyses, for example. However, the proposed methodology should not be seen as exclusive to

the study of ATO system, for it can also be applied to other faceted nanostructured crystalline systems.

## Experimental Section

The ATO nanocrystals were synthesized in a glovebox under a controlled atmosphere by the benzyl alcohol method.<sup>32</sup> For an 18%<sub>atom</sub> Sb doping concentration (nominal composition), a total of 5.47 mmol of SnCl<sub>4</sub> (99.995%) and 1.01 mmol of SbCl<sub>3</sub> (99.99%) were stirred in a vessel with 40 mL of benzyl alcohol, after which the reaction vessel was removed from the glovebox and heated at 150 °C for about 48 h in a silicone bath. ATO nanoparticles were collected by centrifugation, washed twice with tetrahydrofuran, and stocked in a concentrated tetrahydrofuran (THF) dispersion.

TEM samples were prepared by dripping diluted ATO solution onto copper grids covered with a thin amorphous carbon film (~5 nm). HRTEM characterization was performed on a JEM-3010 URP TEM at 300 kV with a LaB<sub>6</sub> electron gun and equipped with a 1024 × 1024 thermoelectrically cooled charge-coupled device (CCD) camera and an X-ray energy-dispersive spectroscopy (XEDS) detector.

Wulff construction<sup>20,21</sup> was applied to build theoretical crystals by using the ab initio calculated surface energies and the SnO<sub>2</sub> P4<sub>2</sub>/mmm crystal structure. HRTEM multislice simulated images of theoretical ATO nanocrystals were obtained by use of JEMS software.<sup>33</sup>

Surface energy calculations<sup>19</sup> for ATO nanocrystals were performed with the CRYSTAL06 program package. Oxygen atoms were described by the standard 6-31G\* basis sets and the tin and antimony centers in the PS-21G\* scheme,<sup>34</sup> where PS stands for Durand-Barthelat's nonrelativistic large effective core potential.<sup>35</sup> Becke's three-parameter hybrid nonlocal exchange functional<sup>36</sup> combined with the Lee–Yang–Parr gradient-corrected correlation functional (B3LYP)<sup>37</sup> was used.

Full optimization of the cell parameters (*a* and *c*) and internal coordinate (*u*) for the bulk SnO<sub>2</sub> was carried out. The low index (110), (101), (100), and (001) surfaces were modeled by unreconstructed (truncated bulk) slab models by use of the calculated equilibrium geometry. Because these surfaces have a different number of atoms in each layer, the low-index surfaces were modeled with different thicknesses in the *z*-direction but were periodic in *x*- and *y*-directions. After the corresponding convergence test on the undoped systems, slab models containing nine SnO<sub>2</sub> layers for the (110), (100), and (101) surfaces and 11 layers for the (001) surface were selected. For the models used here, the top and bottom planes are equivalent in symmetry so the substitution of Sn for Sb atoms was done on both sides of each slab model. Supercells were used to model the lower percentages of doping (~7%). A complete relaxation of all the atoms in each model was performed.

## Results

X-ray diffraction (XRD) analysis of synthesized ATO indicated highly crystalline nanocrystals with SnO<sub>2</sub> cassiterite tetragonal structure (see section S11 in Supporting Information). No other crystalline phases were revealed by the XRD analysis, indicating the complete incorporation of Sb in the SnO<sub>2</sub> structure. The broad XRD peaks indicate small crystalline domains with dimensions of approximately 5 and 4 nm for (110) and (101) planes, respectively, as evaluated by Scherrer's equation, suggesting the presence of elongated crystals.

- (14) Renaud, G.; Lazari, R.; Revenant, C.; Barbier, A.; Noblet, M.; Ulrich, O.; Leroy, F.; Jupille, J.; Borensztein, Y.; Henry, C. R.; Deville, J. P.; Scheurer, F.; Mane-Mane, J.; Fruchart, O. *Science* **2003**, *300* (5624), 1416–1419.
- (15) Morales, E. H.; He, Y.; Vinnichenko, M.; Delley, B.; Diebold, U. *New J. Phys.* **2008**, *10*, 125030.
- (16) Ferrer, D.; Torres-Castro, A.; Gao, X.; Sepulveda-Guzman, S.; Ortiz-Mendez, U.; Jose-Yacamán, M. *Nano Lett.* **2007**, *7* (6), 1701–1705.
- (17) Muller, D. A.; Kourkoutis, L.; Murfitt, M.; Song, J. H.; Hwang, H. Y.; Silcox, J.; Dellby, N.; Krivanek, O. L. *Science* **2008**, *319*, 1073–1076.
- (18) Jia, C. L.; Urban, K. *Science* **2004**, *303*, 2001–2004.
- (19) Beltrán, A.; Andrés, J.; Longo, E.; Leite, E. R. *Appl. Phys. Lett.* **2003**, *83* (4), 635–637.
- (20) Herring, C. *Phys. Rev.* **1951**, *82* (1), 87–93.
- (21) Marks, L. D. *J. Cryst. Growth* **1983**, *61* (3), 556–566.
- (22) Minami, T. *Semicond. Sci. Technol.* **2005**, *20* (4), S35–S44.
- (23) Rakhshani, A. E.; Makdisi, Y.; Ramazaniyan, H. A. *J. Appl. Phys.* **1998**, *83* (2), 1049–1057.
- (24) Granqvist, C. G.; Hultaker, A. *Thin Solid Films* **2002**, *411* (1), 1–5.
- (25) Terrier, C.; Chatelon, J. P.; Roger, J. A. *Thin Solid Films* **1997**, *295* (1–2), 95–100.
- (26) Kowal, A.; Li, M.; Shao, M.; Sasaki, K.; Vukmirovic, M. B.; Zhang, J.; Marinkovic, N. S.; Liu, P.; Frenkel, A. I.; Adzic, R. R. *Nat. Mater.* **2009**, *8* (4), 325–330.
- (27) Lee, K. S.; Park, I. S.; Cho, Y. H.; Jung, D. S.; Jung, N.; Park, H. Y.; Sung, Y. E. *J. Catal.* **2008**, *258* (1), 143–152.
- (28) Dasgupta, S.; Gottschalk, S.; Kruk, R.; Hahn, H. *Nanotechnology* **2008**, *19* (43), 435203.
- (29) Luff, B. J.; Wilkinson, J. S.; Perrone, G. *Appl. Opt.* **1997**, *36* (27), 7066–7072.
- (30) Wang, Y. D.; Djerdj, I.; Antonietti, M.; Smarsly, B. *Small* **2008**, *4* (10), 1656–1660.
- (31) Da Silva, R. O.; Conti, T. G.; De Moura, A. F.; Stroppa, D. G.; Freitas, L. C. G.; Ribeiro, C.; Camargo, E. R.; Longo, E.; Leite, E. R. *ChemPhysChem* **2009**, *10* (5), 841–846.

- (32) Niederberger, M.; Gartweitner, G. *Chem.—Eur. J.* **2006**, *12* (28), 7282–7302.
- (33) Stadelmann, P. A. *Ultramicroscopy* **1987**, *21* (2), 131–145.
- (34) Available at <http://www.crystal.unito.it/>.
- (35) Durand, P.; Barthelat, J. C. *Theor. Chim. Acta* **1975**, *38* (4), 283–302.
- (36) Becke, A. D. *J. Chem. Phys.* **1993**, *98* (7), 5648–5652.
- (37) Lee, C.; Yang, W.; Parr, R. G. *Phys. Rev. B* **1988**, *37* (2), 785–789.

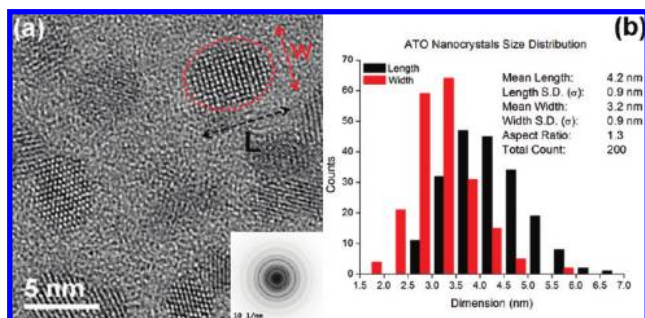


**Figure 1.** Typical HRTEM image of ATO nanocrystals and size distribution histogram. (a) HRTEM image of representative ATO (Sb–SnO<sub>2</sub>) nanocrystals, where the inset shows the electron diffraction pattern and the dashed lines exemplify the measured length and width. (b) Size distribution histogram, where the red and black bars represent the width and length, respectively. The inset text indicates the mean sizes with their respective standard deviations and the aspect ratio for a total count of 200 particles.

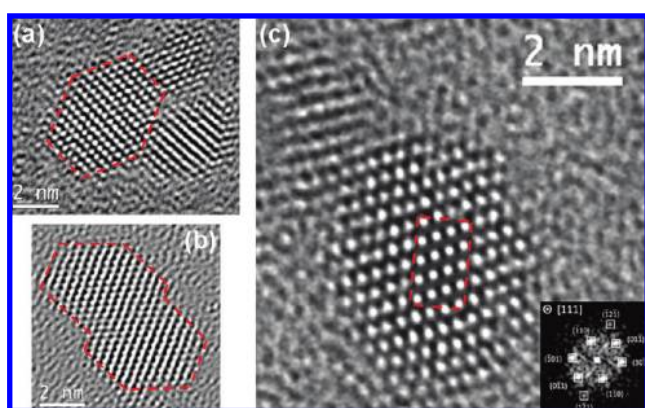


**Figure 2.** HRTEM images of ATO nanocrystals. (a, b) HRTEM images of faceted ATO (Sb–SnO<sub>2</sub>) nanocrystals, showing oriented attachment growth. The red dashed lines highlight the projected facet boundaries. (c) HRTEM image of faceted ATO nanocrystal. The dashed red box indicates the superimposed multislice simulated HRTEM image. (Inset) Fast Fourier Transform, which indicates the particle alignment along the [111] zone axis.

HRTEM images show that the nonaqueous synthesis route produces highly dispersed and crystalline ATO nanoparticles, as presented in Figure 1a. The evaluation of size distribution shown in Figure 1b reveals elongated particles with a mean length of 4.2 nm, mean width of 3.2 nm, and mean aspect ratio of 1.3.

The electron diffraction pattern of ATO nanoparticles depicted in Figure 1a also indicates a SnO<sub>2</sub> cassiterite tetragonal structure with  $P4_2/mnm$  spatial group symmetry. Measured interplanar distances are in excellent agreement with the XRD results and the previously reported crystallographic characterization.<sup>38</sup>

The HRTEM analysis of ATO samples indicated two relevant morphological aspects: (a) the formation of faceted nanocrystals and (b) the occurrence of oriented attachment as the growth mechanism for a significant number of particles, as illustrated in Figure 2a,b. Figure 2c shows a representative HRTEM image of ATO samples and the fast Fourier Transform (FFT), which indicates the particle orientation along the [111] zone axis. An HRTEM multislice simulation of SnO<sub>2</sub>  $P4_2/mnm$  crystal structure under the experimental image conditions is shown in Figure 2c (dashed box). It is important to point out that the reported

(38) McCarthy, G. J.; Welton, J. M. *Powder Diffr.* **1989**, *4* (3), 156–160.

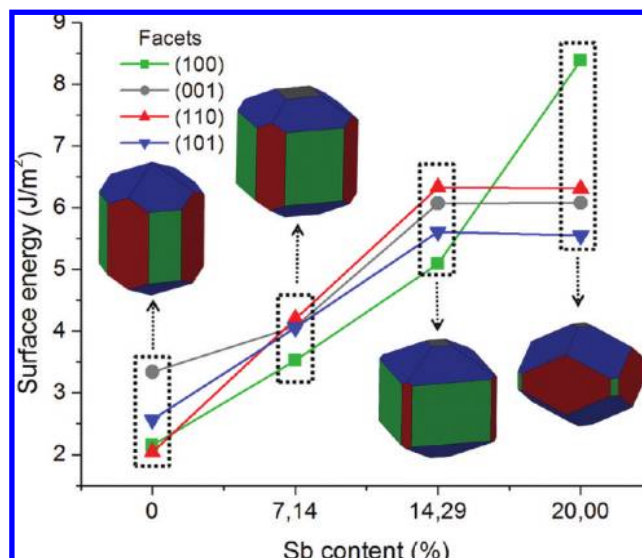


**Figure 3.** Surface energies for different Sb contents and Wulff constructed nanocrystals for each dopant content considering a homogeneous Sb distribution. The figure shows the ab initio calculated surface energies for the selected crystalline planes with different Sb contents. The facets on the constructed Wulff crystals are indicated by a color code.

morphological features of the ATO nanocrystals are directly related to the presence and distribution of Sb dopant. SnO<sub>2</sub> nanocrystals obtained by a similar synthetic route do not present a faceted shape.<sup>39</sup>

Soluble ions play a major role during crystallization, particularly in crystal shape, as previously reported for CaCO<sub>3</sub>.<sup>40</sup> This effect is explained by the reduction of particle surface energy due to the substitution of native surface ions by foreign ones. The analyses suggest that the addition of Sb modifies the SnO<sub>2</sub> surface energy, leading to crystal shape modifications. In order to validate this assumption, the Wulff construction<sup>20,21</sup> was chosen as the model to evaluate ATO nanocrystal faceting based on surface energy ab initio calculations for different exposed crystallographic planes and Sb concentrations.

According to Wulff's rule,<sup>41</sup> which determines the equilibrium crystal shape by minimizing surface energy for a given enclosed volume, the crystal morphology can be thermodynamically predicted by use of the surface energy of different facets. Thus, the crystal shape can be derived from a geometrical construction where the distance of the facet from an arbitrary origin is proportional to the respective crystallographic plane surface energy. The ab initio calculated surface energies for different crystalline planes and Sb concentrations are presented in Figure 3, as well as the Wulff construction for different Sb contents. Due to the substitutional character of Sb in the ATO structure, the dopant concentration is quantized according to available exposed sites.

The results of the calculations shown in Figure 3 indicate that the surface energy for different exposed crystalline planes is highly dependent on the Sb concentration, leading to dependence of the nanocrystal habit on the dopant content. In addition, preferential segregation toward different exposed crystalline planes can be inferred due to modifications of the nanocrystal

(39) Ba, J. H.; Polleux, J.; Antonietti, M.; Niederberger, M. *Adv. Mater.* **2005**, *17* (20), 2509–2512.

(40) Titiloye, J. O.; Parker, S. C.; Mann, S. *J. Cryst. Growth* **1993**, *131*, 533–545.

(41) Wulff, G. Z. *Kryst. Mineral.* **1901**, *34*, 449–530.

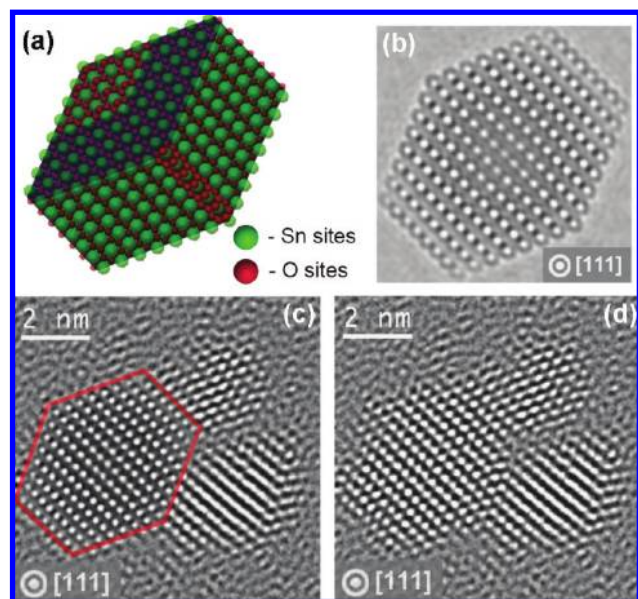


**Figure 4.** Proposed and actual ATO nanocrystals observed along the [111] zone axis. (a) Proposed ATO (Sb–SnO<sub>2</sub>) nanocrystal habit superimposed on its Wulff construction. (b) Multislice simulated HRTEM image obtained from the proposed nanocrystal habit. (c,d) Comparison of the nanocrystal multislice simulated HRTEM nanocrystal image (c) and the experimental HRTEM image (d).

habit as a function of dopant content, especially in highly doped systems. Therefore, both qualitative and quantitative information can be extracted from HRTEM images of faceted and crystalline nanosystems by evaluating the aspect ratio for different crystallographic planes within the Wulff construction.

Based on projected two-dimensional HRTEM images of ATO nanocrystals observed along the [111] zone axis, a hypothetical nanocrystal shape is proposed. The actual HRTEM images provide the exact number of atomic columns on the oriented ATO nanocrystals and hence provide precise information regarding their projected dimensions. In this specific case, the exposed (100), (110), (111), and (101) facets were successfully reconstructed on the basis of the HRTEM image of the particle due to the [111] oriented tetragonal crystalline structure. Only the possibly exposed (001) facet could not be directly evaluated because it does not substantially modify the projected dimensions of the ATO nanoparticle HRTEM image when observed along the [111] zone axis. However, simulated HRTEM images of the proposed nanocrystal atomic arrangement provide information about all the facets considered (see section SI2 in Supporting Information). Thus, it is possible to infer the habit of the actual ATO nanocrystals from an iterative process based on the combined use of HRTEM characterization, Wulff construction, and HRTEM multislice image simulation.

Figure 4a,b presents the proposed ATO nanocrystal atomic arrangement with a superimposed Wulff construction and the multislice simulated HRTEM image,<sup>33</sup> respectively. Figure 4c,d compares the nanocrystal multislice simulated HRTEM image (c) and the experimental image (d). The remarkable agreement between the images supports the proposed nanocrystal habit.

Dimensional analysis of the proposed ATO nanocrystal indicates the surface energy ratio for the different exposed crystallographic planes of the experimental ATO nanocrystals. Therefore, a comparison of these surface energy values and the ab initio calculated ones provides the dopant content on those exposed facets. Table 1 presents the absolute distances of the

**Table 1.** Evaluation of Surface Energy and Sb Content for the Proposed ATO Nanocrystal Habit

exposed plane	distance (nm)	surface energy (J/m <sup>2</sup> )	% <sub>atom</sub> Sb
(001)	1.73	4.68	8.0
(101)	2.08	5.63	14.2
(100)	1.90	5.14	15.3
(110)	2.50	6.76	16.1

proposed Wulff-constructed facets of the ATO nanocrystal, the surface energy values, and the estimated Sb content for the exposed crystalline planes. Both surface energy and dopant content of each facet were evaluated by use of Wulff construction dimensions, mean nanocrystal Sb content retrieved by XEDS measurements, and ab initio calculated surface energies. A detailed description of this methodology is presented in section SI3 of Supporting Information. Finally, the estimated Sb concentrations of the exposed facets of the proposed ATO nanocrystal were quantized on the basis of the available Sn atomic sites on these crystallographic planes. This evaluation of the Sb content on the exposed facets, presented in Table 1, indicates a preferential segregation of Sb toward the (100) and (110) facets and a dopant depletion at the (001) facets of the ATO nanocrystals.

As previously shown, the ATO nanocrystal self-assembling process occurs through oriented attachment (OA) growth.<sup>42–44</sup> OA is a statistical process related to the collision rate among nanocrystals in suspension and to the reduction of surface energy driven by the area minimization of high-energy facets.<sup>45</sup> It has been recently reported as the predominant growth mechanism for an increasing number of materials and has called the attention of scientists as a suitable technique for processing mesocrystals and anisotropic nanomaterials.<sup>46–51</sup> Several growth kinetic models<sup>52,53</sup> have been developed that consider OA as a common step in the nanocrystal growth mechanism, even in systems with high solubility in which Ostwald ripening is the predominant growth mechanism.<sup>54</sup>

Figure 2b shows a pair of coalesced ATO nanocrystals, self-organized through OA growth. This oriented ensemble was evaluated by use of the previously proposed nanocrystal model and simulated HRTEM images in order to investigate the OA growth mechanism. Figure 5a,b presents the atomic arrangement of an ATO nanocrystal ensemble superimposed with its Wulff construction and the results of HRTEM multislice image simulation, respectively. Figure 5c,d compares the multislice simulated HRTEM image of the ensemble (c) and the experimental image (d).

(42) Penn, R. L.; Banfield, J. F. *Am. Mineral.* **1998**, *83*, 1077–1082.

(43) Penn, R. L.; Banfield, J. F. *Science* **1998**, *281*, 969–971.

(44) Penn, R. L.; Banfield, J. F. *Geochim. Cosmochim. Acta* **1999**, *63*, 1549–1557.

(45) Leite, E. R.; Giraldi, T. R.; Pontes, F. M.; Longo, E.; Beltran, A.; Andres, J. *Appl. Phys. Lett.* **2003**, *83*, 1566–1568.

(46) Tang, Z. Y.; Kotov, N. A.; Giersig, M. *Science* **2002**, *297*, 237.

(47) Colfen, H.; Antonietti, M. *Angew. Chem., Int. Ed.* **2005**, *44*, 5576–5591.

(48) Fang, J. X.; Ma, X. N.; Cai, H. H.; Song, X. P.; Ding, B. J. *Nanotechnology* **2006**, *17*, 5841–5845.

(49) Niederberger, M.; Colfen, H. *Phys. Chem. Chem. Phys.* **2006**, *8*, 3271–3287.

(50) Meldrum, F. C.; Colfen, H. *Chem. Rev.* **2008**, *108*, 4332–4432.

(51) Zhou, L.; O'Brien, P. *Small* **2008**, *4*, 1566–1577.

(52) Zhang, H. Z.; Banfield, J. F. *Nano Lett.* **2004**, *4*, 713.

(53) Ribeiro, C.; Lee, E. J. H.; Longo, E.; Leite, E. R. *ChemPhysChem* **2005**, *6*, 690–696.

(54) Ratkovich, A. S.; Penn, R. L. *J. Phys. Chem. C* **2007**, *111*, 14098–14104.

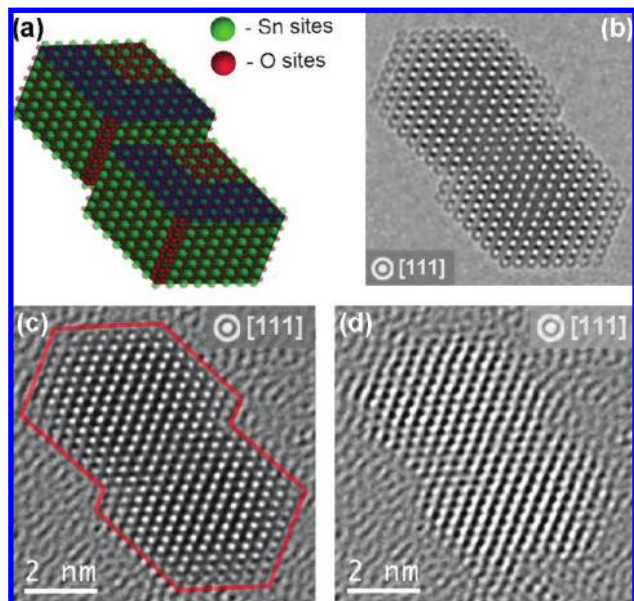


**Figure 5.** Proposed ATO nanocrystal ensemble and its simulated HRTEM image. (a) Atomic arrangement of the ATO (Sb–SnO<sub>2</sub>) nanocrystal ensemble superimposed on its Wulff construction. (b) Multislice simulated HRTEM image obtained from the proposed nanocrystal ensemble. (c, d) Comparison of the simulated nanocrystal image (c) and the experimental image (d).

The remarkable agreement between the experimental HRTEM image and the simulated image of the proposed ATO nanocrystal assembly allows for an accurate evaluation of the OA mechanism. [100] and [101] were observed as the preferential growth directions for the ATO nanoparticles. Figure 5c corresponds to an example of (100) facet oriented attachment. The OA growth process along the [100] and [101] directions is congruent with the predicted attachment configurations (see section SI4 in Supporting Information) and with the higher expected collision rate for the (100) and (101) facets as a result of their larger exposed facet area. In the proposed nanocrystal habit, more than 78% of the total surface area corresponds to (100) and (101) facets.

The combined use of HRTEM characterization, HRTEM multislice image simulation, and ab initio calculations provided information on the 3D habit and surface chemical composition of faceted nanocrystals by correlation of the crystal faceting and the dopant-dependent surface energy of exposed facets.

### Concluding Remarks

Based on indirect quantitative measurements, this methodology is a novel approach for the evaluation of surface dopant distribution on nanoparticles. It is a powerful tool for the analysis of nanocrystals, where usual quantitative techniques such as X-ray photoelectron spectroscopy (XPS), X-ray energy-dispersive spectroscopy (XEDS), high-angle annular dark field (HAADF), and electron energy loss spectroscopy (EELS) would require a much greater effort and/or would be restricted by system dimensions and/or small atomic weight differences between the material elements.<sup>55</sup>

In addition, the combined use of surface energy ab initio calculations and Wulff construction applied to nanocrystal modeling was applied successfully to study the oriented attachment growth mechanism in ATO nanocrystals and can be used to carry out such studies in a number of nanostructured systems. Modeling hypothetical nanocrystals as building blocks with known surface energy distribution and faceting enables one to produce a three-dimensional description of the oriented attachment growth mechanism, which can be further investigated by HRTEM imaging and HRTEM multislice image simulation.

**Acknowledgment.** We acknowledge the financial support of the Brazilian research funding agencies FAPESP, CNPq, and FINEP.

**Supporting Information Available:** XRD characterization, HRTEM image simulation for different (001) nanocrystal faceting, XEDS and dopant distribution analyses, and OA evaluation. This material is available free of charge via the Internet at <http://pubs.acs.org>.

JA905896U

(55) Sun, K.; Liu, J.; Browning, N. D. *J. Catal.* **2002**, *205*, 266–277.